Search for neutrino-induced particle showers with IceCube-40

Aartsen, M.G.; Abbasi, R.; Ackermann, M.; Admas, J.; Aguilar, J.A.; Ahlers, M.; Altmann, D.; Arguelles, C.; Arlen, T.C.; Auffenberg, J.; Bai, X.; Baker, M.; Koskinen, David Jason; Sarkar, Subir; Larson, Michael James

Search for neutrino-induced particle showers with IceCube-40

M. G. Aartsen,[2] R. Abbasi,[29] M. Ackermann,[45] J. Adams,[15] J. A. Aguilar,[23] M. Ahlers,[29] D. Altmann,[22] C. Arguelles,[29] T. C. Arlen,[42] J. Auffenberg,[29] X. Bai,[33,*] M. Baker,[29] S. W. Barwick,[25] V. Baum,[30] R. Bay,[7] J. J. Beatty,[17,18] J. Becker Tjus,[10] K.-H. Becker,[44] S. BenZvi,[29] P. Berghaus,[45] D. Berley,[16] E. Bernardini,[45] A. Bernhard,[32] D. Z. Besson,[27] G. Binder,[8,7] D. Bindig,[44] M. Bissok,[1] E. Blaufuss,[16] J. Blumenthal,[1] D. J. Boersma,[43] C. Bohm,[36] D. Bose,[38] S. Böser,[11] O. Botner,[43] L. Brayeur,[13] H.-P. Bretz,[45] A. M. Brown,[15] R. Bruijn,[26] J. Casey,[5] M. Casier,[13] D. Chirkin,[29] A. Christov,[23] B. Christy,[16] K. Clark,[39] L. Classen,[22] F. Clevermann,[20] S. Coenders,[1] S. Cohen,[26] D. F. Cowen,[42,41] A. H. Cruz Silva,[45] M. Danninger,[36] J. Daughhetee,[5] J. C. Davis,[17] M. Day,[29] J. P. A. M. de André,[42] C. De Clercq,[13] S. De Ridder,[24] P. Desiati,[29] K. D. de Vries,[13] M. de With,[9] T. DeYoung,[42] J. C. Díaz-Vélez,[29] M. Dunkman,[42] R. Eagan,[42] B. Eberhardt,[30] B. Eichmann,[10] J. Eisch,[29] S. Euler,[1] P. A. Evenson,[33] O. Fadiran,[29] A. R. Fazely,[6] A. Fedynitch,[10] J. Feintzeig,[29] T. Feusels,[24] K. Filimonov,[7] C. Finley,[36] T. Fischer-Wasels,[44] S. Flis,[36] A. Franckowiak,[11] K. Frantzen,[20] T. Fuchs,[20] T. K. Gaisser,[33] J. Gallagher,[28] L. Gerhardt,[8,7] L. Gladstone,[29] T. Glüsenkamp,[45] A. Goldschmidt,[8] G. Golup,[13] J. G. Gonzalez,[33] J. A. Goodman,[16] D. Góra,[22] D. T. Grandmont,[21] D. Grant,[21] P. Gretskov,[1] J. C. Groh,[42] A. Groß,[32] C. Ha,[8,7] A. Haj Ismail,[24] P. Hallen,[1] A. Hallgren,[43] F. Halzen,[29] K. Hanson,[12] D. Hebecker,[11] D. Heereman,[12] D. Heinen,[1] K. Helbing,[44] R. Hellauer,[16] S. Hickford,[15,†] G. C. Hill,[2] K. D. Hoffman,[16] R. Hoffmann,[44] A. Homeier,[11] K. Hoshina,[29] F. Huang,[42] W. Huelsnitz,[16] P. O. Hulth,[36] K. Hultqvist,[36] S. Hussain,[33] A. Ishihara,[14] E. Jacobi,[45] J. Jacobsen,[29] K. Jagielski,[1] G. S. Japaridze,[4] K. Jero,[29] O. Jlelati,[24] B. Kaminsky,[45] A. Kappes,[22] T. Karg,[45] A. Karle,[29] M. Kauer,[29] J. L. Kelley,[29] J. Kiryluk,[37] J. Kläs,[44] S. R. Klein,[8,7] J.-H. Köhne,[20] G. Kohnen,[31] H. Kolanoski,[9] L. Köpke,[30] C. Kopper,[29] S. Kopper,[44] D. J. Koskinen,[19] M. Kowalski,[11] M. Krasberg,[29] A. Kriesten,[1] K. Krings,[1] G. Kroll,[30] J. Kunnen,[13] N. Kurahashi,[29] T. Kuwabara,[33] M. Labare,[24] H. Landsman,[29] M. J. Larson,[40] M. Lesiak-Bzdak,[37] M. Leuermann,[1] J. Leute,[32] J. Lünemann,[30] O. Macías,[15] J. Madsen,[35] G. Maggi,[13] R. Maruyama,[29] K. Mase,[14] H. S. Matis,[8] F. McNally,[29] K. Meagher,[16] M. Merck,[29] T. Meures,[12] S. Miarecki,[8,7] E. Middell,[45,‡] N. Milke,[20] J. Miller,[13] L. Mohrmann,[45] T. Montaruli,[23] R. Morse,[29] R. Nahnhauer,[45] U. Naumann,[44] H. Niederhausen,[37] S. C. Nowicki,[21] D. R. Nygren,[8] A. Obertacke,[44] S. Odrowski,[21] A. Olivas,[16] A. Omairat,[44] A. O'Murchadha,[12] T. Palczewski,[40] L. Paul,[1] J. A. Pepper,[40] C. Pérez de los Heros,[43] C. Pfendner,[17] D. Pieloth,[20] E. Pinat,[12] J. Posselt,[44] P. B. Price,[7] G. T. Przybylski,[8] M. Quinnan,[42] L. Rädel,[1] M. Rameez,[23] K. Rawlins,[3] P. Redl,[16] R. Reimann,[1] E. Resconi,[32] W. Rhode,[20] M. Ribordy,[26] M. Richman,[16] B. Riedel,[29] S. Robertson,[2] J. P. Rodrigues,[29] C. Rott,[38] T. Ruhe,[20] B. Ruzybayev,[33] D. Ryckbosch,[24] S. M. Saba,[10] H.-G. Sander,[30] M. Santander,[29] S. Sarkar,[19,34] K. Schatto,[30] F. Scheriau,[20] T. Schmidt,[16] M. Schmitz,[20] S. Schoenen,[1] S. Schöneberg,[10] A. Schönwald,[45] A. Schukraft,[1] L. Schulte,[11] O. Schulz,[32] D. Seckel,[33] Y. Sestayo,[32] S. Seunarine,[35] R. Shanidze,[45] C. Sheremata,[21] M. W. E. Smith,[42] D. Soldin,[44] G. M. Spiczak,[35] C. Spiering,[45] M. Stamatikos,[17,§] T. Stanev,[33] N. A. Stanisha,[42] A. Stasik,[11] T. Stezelberger,[8] R. G. Stokstad,[8] A. Stößl,[45] E. A. Strahler,[13] R. Ström,[43] N. L. Strotjohann,[11] G. W. Sullivan,[16] H. Taavola,[43] I. Taboada,[5] A. Tamburro,[33] A. Tepe,[44] S. Ter-Antonyan,[6] G. Tešić,[42] S. Tilav,[33] P. A. Toale,[40] M. N. Tobin,[29] S. Toscano,[29] M. Tselengidou,[22] E. Unger,[10] M. Usner,[11] S. Vallecorsa,[23] N. van Eijndhoven,[13] A. Van Overloop,[24] J. van Santen,[29] M. Vehring,[1] M. Voge,[11] M. Vraeghe,[24] C. Walck,[36] T. Waldenmaier,[9] M. Wallraff,[1] Ch. Weaver,[29] M. Wellons,[29] C. Wendt,[29] S. Westerhoff,[29] B. Whelan,[2] N. Whitehorn,[29] K. Wiebe,[30] C. H. Wiebusch,[1] D. R. Williams,[40] H. Wissing,[16] M. Wolf,[36] T. R. Wood,[21] K. Woschnagg,[7] D. L. Xu,[40] X. W. Xu,[6] J. P. Yanez,[45] G. Yodh,[25] S. Yoshida,[14] P. Zarzhitsky,[40] J. Ziemann,[20] S. Zierke,[1] and M. Zoll[36]

(IceCube Collaboration)

[1]III. Physikalisches Institut, RWTH Aachen University, D-52056 Aachen, Germany
[2]School of Chemistry and Physics, University of Adelaide, Adelaide SA, 5005 Australia
[3]Department of Physics and Astronomy, University of Alaska Anchorage, 3211 Providence Drive, Anchorage, Alaska 99508, USA
[4]CTSPS, Clark-Atlanta University, Atlanta, Georgia 30314, USA
[5]School of Physics and Center for Relativistic Astrophysics, Georgia Institute of Technology, Atlanta, Georgia 30332, USA
[6]Department of Physics, Southern University, Baton Rouge, Louisiana 70813, USA
[7]Department of Physics, University of California, Berkeley, California 94720, USA
[8]Lawrence Berkeley National Laboratory, Berkeley, California 94720, USA
[9]Institut für Physik, Humboldt-Universität zu Berlin, D-12489 Berlin, Germany
[10]Fakultät für Physik and Astronomie, Ruhr-Universität Bochum, D-44780 Bochum, Germany
[11]Physikalisches Institut, Universität Bonn, Nussallee 12, D-53115 Bonn, Germany
[12]Université Libre de Bruxelles, Science Faculty CP230, B-1050 Brussels, Belgium
[13]Vrije Universiteit Brussel, Dienst ELEM, B-1050 Brussels, Belgium
[14]Department of Physics, Chiba University, Chiba 263-8522, Japan

[15]*Department of Physics and Astronomy, University of Canterbury, Private Bag 4800,*
Christchurch, New Zealand
[16]*Department of Physics, University of Maryland, College Park, Maryland 20742, USA*
[17]*Department of Physics and Center for Cosmology and Astro-Particle Physics, Ohio State University,*
Columbus, Ohio 43210, USA
[18]*Department of Astronomy, Ohio State University, Columbus, Ohio 43210, USA*
[19]*Niels Bohr Institute, University of Copenhagen, DK-2100 Copenhagen, Denmark*
[20]*Department of Physics, TU Dortmund University, D-44221 Dortmund, Germany*
[21]*Department of Physics, University of Alberta, Edmonton, Alberta, Canada T6G 2E1*
[22]*Erlangen Centre for Astroparticle Physics, Friedrich-Alexander-Universität Erlangen-Nürnberg,*
D-91058 Erlangen, Germany
[23]*Département de physique nucléaire et corpusculaire, Université de Genève,*
CH-1211 Genève, Switzerland
[24]*Department of Physics and Astronomy, University of Gent, B-9000 Gent, Belgium*
[25]*Department of Physics and Astronomy, University of California, Irvine, California 92697, USA*
[26]*Laboratory for High Energy Physics, École Polytechnique Fédérale, CH-1015 Lausanne, Switzerland*
[27]*Department of Physics and Astronomy, University of Kansas, Lawrence, Kansas 66045, USA*
[28]*Department of Astronomy, University of Wisconsin, Madison, Wisconsin 53706, USA*
[29]*Department of Physics and Wisconsin IceCube Particle Astrophysics Center, University of Wisconsin,*
Madison, Wisconsin 53706, USA
[30]*Institute of Physics, University of Mainz, Staudinger Weg 7, D-55099 Mainz, Germany*
[31]*Université de Mons, 7000 Mons, Belgium*
[32]*T.U. Munich, D-85748 Garching, Germany*
[33]*Bartol Research Institute and Department of Physics and Astronomy, University of Delaware, Newark,*
Delaware 19716, USA
[34]*Department of Physics, University of Oxford, 1 Keble Road, Oxford OX1 3NP, United Kingdom*
[35]*Department of Physics, University of Wisconsin, River Falls, Wisconsin 54022, USA*
[36]*Oskar Klein Centre and Department of Physics, Stockholm University, SE-10691 Stockholm, Sweden*
[37]*Department of Physics and Astronomy, Stony Brook University, Stony Brook,*
New York 11794-3800, USA
[38]*Department of Physics, Sungkyunkwan University, Suwon 440-746, Korea*
[39]*Department of Physics, University of Toronto, Toronto, Ontario, Canada, M5S 1A7*
[40]*Department of Physics and Astronomy, University of Alabama, Tuscaloosa, Alabama 35487, USA*
[41]*Department of Astronomy and Astrophysics, Pennsylvania State University, University Park,*
Pennsylvania 16802, USA
[42]*Department of Physics, Pennsylvania State University, University Park,*
Pennsylvania 16802, USA
[43]*Department of Physics and Astronomy, Uppsala University, Box 516, S-75120 Uppsala, Sweden*
[44]*Department of Physics, University of Wuppertal, D-42119 Wuppertal, Germany*
[45]*DESY, D-15735 Zeuthen, Germany*
(Received 30 November 2013; published 1 May 2014)

We report on the search for neutrino-induced particle showers, so-called cascades, in the IceCube-40 detector. The data for this search were collected between April 2008 and May 2009 when the first 40 IceCube strings were deployed and operational. Three complementary searches were performed, each optimized for different energy regimes. The analysis with the lowest energy threshold (2 TeV) targeted atmospheric neutrinos. A total of 67 events were found, consistent with the expectation of 41 atmospheric muons and 30 atmospheric neutrino events. The two other analyses targeted a harder, astrophysical neutrino flux. The analysis with an intermediate threshold of 25 TeV leads to the observation of 14 cascadelike events, again consistent with the prediction of 3.0 atmospheric neutrino and 7.7 atmospheric muon events. We hence set an upper limit of $E^2 \Phi_{lim} \leq 7.46 \times 10^{-8}$ GeV sr^{-1} s^{-1} cm^{-2} (90% C.L.) on the diffuse flux from astrophysical neutrinos of all neutrino flavors, applicable to the energy range 25 TeV to 5 PeV, assuming an E_ν^{-2} spectrum and a neutrino flavor ratio of $1:1:1$ at the Earth. The third analysis

[*]Also at Physics Department, South Dakota School of Mines and Technology, Rapid City, SD 57701, USA.
[†]Corresponding author.
stephanie.v.hickford@gmail.com
[‡]Corresponding author.
eike.middell@desy.de
[§]Also at NASA Goddard Space Flight Center, Greenbelt, MD 20771, USA.

utilized a larger and optimized sample of atmospheric muon background simulation, leading to a higher energy threshold of 100 TeV. Three events were found over a background prediction of 0.04 atmospheric muon events and 0.21 events from the flux of conventional and prompt atmospheric neutrinos. Including systematic errors this corresponds to a 2.7σ excess with respect to the background-only hypothesis. Our observation of neutrino event candidates above 100 TeV complements IceCube's recently observed evidence for high-energy astrophysical neutrinos.

I. INTRODUCTION

One century after the discovery of cosmic rays the search for their sources is still ongoing. Astrophysical objects which are either confirmed or expected to be able to accelerate hadrons to the observed energies include supernova remnants [1], active galactic nuclei, gamma-ray bursts, and shocks in star formation regions of galaxies. The cosmic-ray nuclei interact with ambient matter and radiation fields close to their source [2]. Charged pions produced in these interactions decay into neutrinos. Therefore, the detection of high-energy neutrinos from such objects provides a unique possibility to identify individual astrophysical objects as cosmic-ray sources. However, low fluxes and small interaction probabilities make the detection of high-energy neutrinos challenging. To date no astrophysical object has been conclusively identified as a source of TeV neutrinos. Previous searches have established limits enabling astrophysical models to be constrained [3,4].

While individual neutrino sources might be too weak to be detectable with current instruments, they would still contribute to a collective astrophysical neutrino flux. Fermi shock acceleration is thought to be the main acceleration mechanism for cosmic-ray nuclei and therefore a power-law spectrum with an index of about -2 is expected for the nuclei in the interaction regions where the neutrinos are produced. Based on the energy density of ultrahigh-energy cosmic rays and assuming the cosmic-ray sources are transparent, the all-flavor diffuse neutrino flux can be constrained theoretically to be lower than the Waxman-Bahcall bound of $E_\nu^2 \Phi \lesssim 3 \times 10^{-8}$ GeV sr^{-1} s^{-1} cm^{-2} [5,6]. As neutrinos are assumed to originate mainly from pion decays, at the source a flavor ratio of $\nu_e : \nu_\mu : \nu_\tau = 1:2:0$ is expected. This ratio would transform to $1:1:1$ on Earth due to neutrino oscillations [7,8]. However, observing unequal or energy-dependent flavor contributions would be interesting, since for example the flavor ratio is sensitive to the assumed production mechanism at the source [9].

Recently, evidence for this diffuse astrophysical neutrino flux was found. Its all-flavor intensity is estimated to be $E_\nu^2 \Phi = (3.6 \pm 1.2) \times 10^{-8}$ GeV sr^{-1} s^{-1} cm^{-2} with indications for a cutoff at ~ 2 PeV. It is consistent with an isotropic flux and a flavor ratio of $1:1:1$ ([10,11] and Fig. 1).

In order to measure the diffuse astrophysical neutrino flux at TeV energies, it has to be separated from two main sources of background, which both originate from the

Earth's atmosphere. These are atmospheric muons and neutrinos produced in cosmic-ray air showers. The atmospheric neutrino flux has two components. The so-called conventional atmospheric neutrinos are produced in decays of pions and kaons. Their intensity is well measured up to 6 TeV for ν_e and up to 400 TeV for ν_μ [12,13]. At higher energies the poor knowledge of the composition of the cosmic-ray flux, creating the neutrinos, causes significant uncertainties on the intensity. The spectrum of the conventional atmospheric neutrinos is steeper than the cosmic-ray spectrum due to pion and kaon energy losses in the atmosphere. The second component originates from the decay of charmed mesons, which have lifetimes several orders of magnitude smaller than charged pions and kaons. Accordingly, neutrinos from these decays are called prompt atmospheric neutrinos. Because of the short lifetime of the parent mesons the energy spectrum of the prompt atmospheric neutrinos is expected to follow the spectrum of the cosmic rays that create them. However, their intensity has never been measured and uncertainties in the relevant
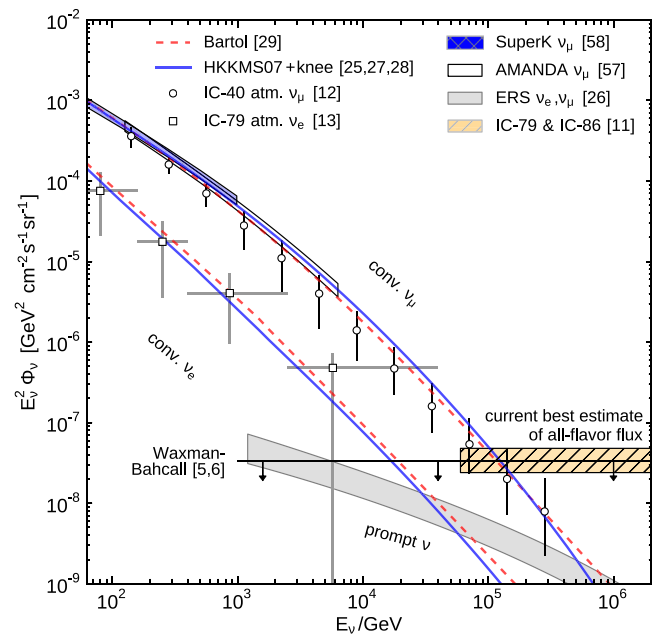

FIG. 1 (color online). Neutrino energy spectrum above 100 GeV. The theoretical predictions and measurements for the atmospheric neutrino flux are shown, as well as the current estimate for the diffuse astrophysical neutrino flux.

production cross sections lead to large uncertainties in the predicted flux. The presence of a prompt neutrino component, like an astrophysical neutrino component, introduces a break into the neutrino energy spectrum. Given the large uncertainties in the prompt neutrino predictions, identification and separation of the astrophysical and prompt components needs to be made through their respective spectral signatures (see Fig. 1).

The IceCube Neutrino Observatory is located at the South Pole and is the first kilometer-scale Cherenkov neutrino telescope. An optical sensor array observes the Cherenkov radiation from secondary charged particles produced in neutrino interactions deep in the ice. These are dominantly neutrino-nucleon interactions except for the Glashow resonance [14] for electron antineutrinos at 6.3 PeV. Based on the signature of the neutrino interaction, which depends on the flavor of the incident neutrino and the type of the interaction, two main detection channels exist. Searches in the muon channel look for charged-current muon neutrino interactions. These have a muon in the final state whose direction is reconstructible with a resolution of about 1° [15]. The large muon range also allows one to detect neutrino interactions outside the instrumented volume. The cascade channel comprises all other interaction scenarios which have particle showers in the final state. Above PeV energies charged-current ν_τ interactions exhibit more complex event signatures, for which tailored analyses are developed. But at TeV energies ν_τ can also be detected through the cascade channel. Consequently, an astrophysical flux with equal neutrino flavor contributions would yield more cascade than track events starting inside of IceCube. If the neutrino interaction happens inside the detector, the Cherenkov light yield of particle showers scales nearly linearly with the deposited energy, leading to an energy resolution that is better than in the muon channel. On the other hand the angular resolution is rather poor (> 10° for the completed IceCube detector). Overall, the cascade channel is best suited for searches for diffuse astrophysical neutrinos in which the neutrino energy measurement is more important than pointing capabilities [16].

This paper presents searches for neutrino-induced cascades in one year of data taken during the construction phase of IceCube, when about half the detector was operational (IceCube-40). The main objective of the searches was to identify an astrophysical flux of neutrinos. In addition, a sensitivity to atmospheric neutrinos in the few TeV energy range was maintained to allow a validation of the anticipated backgrounds in the data set.

A 2.7σ excess of events above 100 TeV was found, compatible with the all-flavor astrophysical diffuse neutrino flux estimate obtained in IceCube's high-energy starting events analysis [11]. In comparison to that analysis, the IceCube-40 cascade analysis provides an event sample with unprecedented low background contamination between 100 and 200 TeV. This is possible because both

searches employed rather different event selection strategies. Methods outlined in this paper also prove powerful in cascade searches with later IceCube configurations [17,18].

The paper is organized as follows: The IceCube detector and IceCube-40 data set are described in Sec. II. The simulation used is presented in Sec. III followed by a description of the cascade reconstruction in Sec. IV. The details of the event selection and expected sensitivity are presented in Sec. V. A survey of the systematic uncertainties follows in Sec. VI before the results and implications are discussed in Sec. VII. A conclusion is given in Sec. VIII.

II. THE ICECUBE DETECTOR

The IceCube Neutrino Observatory [19] consists of an in-ice array of optical sensors and a complementary surface air shower detector called IceTop. The analyses presented here utilized only the in-ice component so the following detector description will be limited to that.

The optical sensors, called digital optical modules (DOMs) [20], are sensitive to Cherenkov photons between 350 and 650 nm. The DOMs are deployed between depths of 1450 and 2450 m and are attached to strings that are formed by the readout cables. Each string has 60 DOMs attached. The vertical string spacing of the DOMs is approximately 17 m and the horizontal spacing between the strings is approximately 125 m. The data for this analysis were collected between April 2008 and May 2009 with a total of 367.1 days live time. In this period 40 strings were deployed and operational. The detector layout is shown in Fig. 2. Before IceCube's completion in 2010, the IceCube-59 and IceCube-79 configurations took data with 59 and 79 deployed strings, respectively.

Each DOM consists of a 25 cm diameter photomultiplier tube (PMT) [21], made by Hamamatsu Photonics, and a data acquisition system housed within a pressure sphere made of 13 mm thick borosilicate glass. The PMT's dynamic range is 200 photoelectrons per 15 ns and it is designed to accurately record the amplitudes and widths of the pulses with a timing resolution of 5 ns. Their peak quantum efficiency is approximately 25% and they are operated at a gain of 10^7 to resolve single photoelectrons.

The time-resolved PMT signal (waveform) is digitized in the DOM. For this purpose two digitization devices are available on the DOM mainboard: two analog transient waveform digitizers (ATWDs) and a fast analog-to-digital converter (fADC). The ATWDs have three channels operated in parallel at different gains to provide a large dynamic range (a fourth channel is used only for calibration purposes). Because of scattering in the ice the arrival times of photons emitted at the same point and time can vary by microseconds. The ATWDs provide a sampling rate of 300 Megasamples/s over a time window of 425 ns allowing them to record the earliest photons (i.e. those least affected by scattering in the ice) with high precision. The second digitizer, the fADC, has a coarser sampling of 40 Megasamples/s recording data over
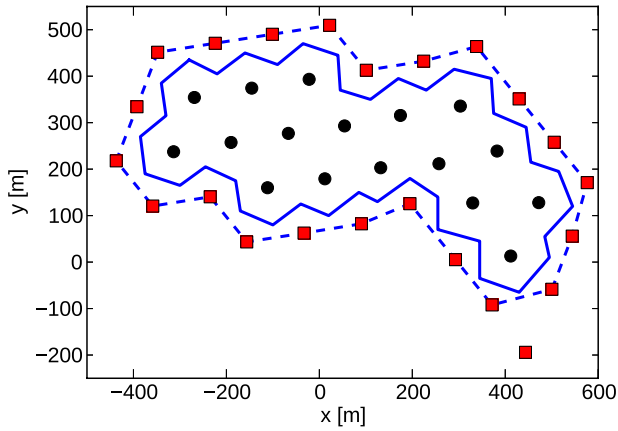
FIG. 2 (color online).   The IceCube-40 detector configuration as viewed from above. The circles and squares are the positions of the strings, which are deployed vertically into the ice. The point $(x, y) = (0, 0)$ is the center of the complete 86-string detector. Particle showers with reconstructed vertices inside the instrumented volume are called contained events. The analyses presented in this work reject noncontained events in order to suppress atmospheric muons that enter the detector from the outside. The blue dashed and solid lines show the two differently tight containment requirements that are used. The strings denoted by red squares form the outer layer of the detector. They are used to veto incident atmospheric muons.

a longer time period for photons with larger delays of up to 6.4 μs. In order to reduce data readout volume due to noise, in IceCube-40 a local coincidence criterion is required. Only if a neighboring DOM on the same string also detects light within the local coincidence time window of ± 1000 ns, the PMT response is digitized, time stamped, and transmitted to the surface for analysis. The surface data acquisition system combines the individual PMT responses and forms events when one of the several possible triggering criteria is fulfilled.

The trigger requirement for the IceCube-40 cascade search was the simple multiplicity trigger, which requires that eight DOMs were hit within a 5000 ns time window. The data rate for IceCube-40 from this trigger was approximately 1000 Hz.

III. SIMULATION

Interactions of all flavors of neutrinos were simulated to model atmospheric and astrophysical neutrinos. The NUGEN software package maintained by the IceCube Collaboration was used. It is based on the ANIS [22] neutrino generator, which produces neutrinos isotropically over the Earth's surface and propagates them to interact in or near the detector volume. Neutrino attenuation and ν_τ regeneration are accounted for using the preliminary reference Earth model [23]. CTEQ5 structure functions [24] were used to model the deep-inelastic neutrino-nucleon scattering cross section.

Throughout this paper the diffuse astrophysical neutrino flux is simulated isotropically, with a flavor ratio of $1:1:1$ and, if not stated otherwise, with an unbroken power-law spectrum with index of -2 and an all-flavor intensity of 3.6×10^{-8} GeV sr^{-1} s^{-1} cm^{-2}.

Rate predictions for the atmospheric neutrinos are based on the HKKMS07 model [25] for conventional atmospheric neutrinos and the ERS model [26] for prompt atmospheric neutrinos. Extrapolations of the original calculations to higher energies provide rate predictions at the energy range relevant to this work. The steepening of the cosmic-ray spectrum around a few PeV (the so-called "knee") causes a similar feature in the atmospheric neutrino spectrum which is not accounted for in the HKKMS07 model. A modification to the HKKMS07 model [27,28] was applied to account for the knee. For one of the presented analyses the Bartol model [29] was used to estimate the conventional atmospheric neutrino flux. Compared to the modified HKKMS07 model it predicts a higher ν_e contribution (see Fig. 1).

The propagation of muons and taus through the detector and their energy losses were simulated using the MMC program [30] and the cascade simulation inside the detector was handled by the CMC program [31]. Neutrino-induced cascades below a threshold of 1 TeV were simulated as pointlike light sources, emitting an angular Cherenkov light profile typical of an electromagnetic shower [32]. Cascades of higher energies are split into segments along the direction of the shower development. Each cascade segment is then approximated by a pointlike subshower with a light yield proportional to the light yield in the corresponding segment of the electromagnetic cascade. The elongation of electromagnetic cascades due to the suppression of bremsstrahlung and pair production cross sections above PeV energies (Landau-Pomeranchuck-Midgal effect [33]) is accounted for. Hadronic cascades are simulated as electromagnetic cascades with a smaller light yield per deposited energy to account for the neutral shower components which do not generate Cherenkov light [34].

The contribution from atmospheric muon events is estimated from simulations done with a modified version [35,36] of the CORSIKA air shower simulation software [37]. A large number of background events must be generated due to the high background suppression that is necessary to reach an event sample dominated by neutrinos. Providing a large background sample is computationally challenging, mostly because of the sheer number of air showers needed but also due to the simulation of light propagation in the optically inhomogeneous ice. The figure of merit used to quantify the statistics of a simulated data sample is the effective live time $T_{\rm eff}$, i.e. the time that one would have to run the real experiment to obtain the same statistical error as in the simulated data set.

The chemical composition of the cosmic rays is important for an estimate of the muon background. Previous
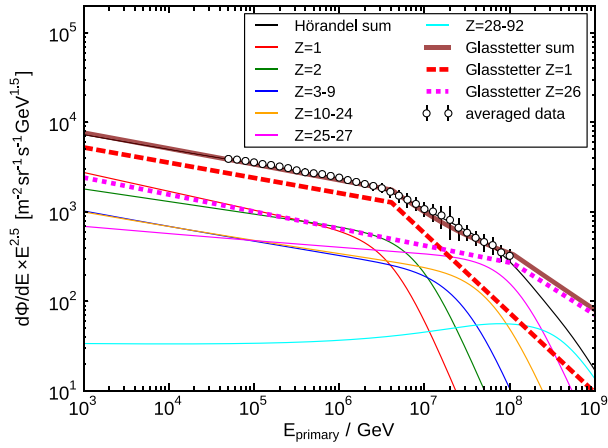
FIG. 3 (color online). The cosmic-ray spectrum is modeled with two broken power laws for proton and iron (red and magenta dashed lines, respectively). Their parameters are taken from Ref. [38]. The Hörandel model and the data from which it has been derived are shown for comparison (both taken from [39]). The Hörandel model comprises components for each element from hydrogen up to iron illustrated by solid lines.

cascade searches [40] have shown that protons are of prime importance. Proton primaries produce lower multiplicities of muons with higher individual energies than heavier primaries. Compared to air showers induced by heavier elements, which typically lead to muon bundles reaching the detector, proton showers are more likely to generate single high-energy muons. If such a high-energy muon has a single catastrophic energy loss, then the relative light
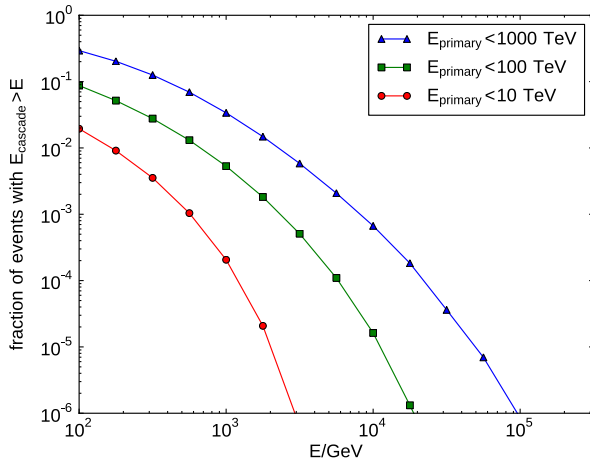

FIG. 4 (color online). Proton air showers are simulated according to the Glasstetter spectrum illustrated in Fig. 3. Bremsstrahlung cascades from muons originating in these showers are studied in order to assess the probability to obtain a bremsstrahlung cascade bright enough to pass event selection cuts from air showers below a given energy threshold. The plot shows the fraction of proton air showers with primary energy E_{primary} below 10, 100, 1000 TeV that exhibit catastrophic energy losses of E_{cascade} above a given energy.

yield between shower and muon can make the resulting event signature look showerlike.

We use a simplified cosmic-ray composition model in our simulation that nevertheless reflects these qualitative differences between light and heavy elements. This two-component model considers only the two extrema of cosmic-ray composition and comprises two broken power laws, one for the proton and one for the iron spectrum, respectively (see [38] and Fig. 3). The mean logarithmic mass of the all-particle spectrum formed from the sum of the two power laws is compatible with measurements of this quantity by air shower experiments [39].

The created background sample provides more than a year of effective live time above an energy per nucleon threshold of about $E/A > 90$ TeV. Below this threshold the statistics drop rather quickly and these low energetic events are underrepresented in the event sample. However, the risk of underestimating the background is low, since the fraction of air showers with a primary energy below 90 TeV which exhibit bremsstrahlung losses of 2 TeV (10 TeV) is only 1.8×10^{-3} (1.6×10^{-5}) (see Fig. 4).

IV. RECONSTRUCTION OF PARTICLE SHOWERS

Cherenkov light, emitted by charged particles, traverses the optically inhomogeneous detector material and is then sampled by the three-dimensional IceCube array with nanosecond precision. Hence, the light's arrival times and amplitudes are the sole available information on any particle interaction in the detector. Previous analyses relied on reconstruction algorithms that used only parts of this information, i.e. by considering only the integrated amplitude of all light reaching a DOM or by using only the arrival time of the first photon. A new algorithm CREDO was developed. By using the waveform information CREDO is able to reconstruct not only the interaction vertex and the deposited energy but also the direction of the incident neutrino. CREDO is the first IceCube cascade reconstruction algorithm which is able to estimate the direction of the neutrino. The measurement process is described with a probabilistic model and a maximum likelihood estimator allows information on the vertex of the neutrino interaction, the neutrino direction and the deposited energy to be inferred.

CREDO considers the information on an event in the form of time intervals $(t, t + \Delta t)$ in which a DOM at position $\vec{x}$ recorded a given amount of charge n. Formally, the event is then described with the set $\{n_i(\vec{x}, t, \Delta t)\}$, where the index i enumerates all such time intervals in all DOMs. It should be noted that this set also contains time intervals in which no charge has been recorded, since these time intervals also carry constraining information. The particle showers are modeled as pointlike Cherenkov emitters, in the same way as they are described in simulation. A particle shower is then fully specified by seven parameters $\alpha = (t, x, y, z, \theta, \phi, E)$: the time and position of the vertex,

two angles for the direction of the neutrino and the deposited energy. The scattering and absorption of light in the Antarctic ice are depth dependent. The PHOTONICS package [41] is used to calculate the light propagation in the ice and to create tables with light arrival times and amplitudes as a function of the depth and the relative position between particle shower and DOM. In order to avoid binning effects the table values are interpolated by multidimensional spline fits [42] prior to being used in the reconstruction.

The PHOTONICS tables are used to calculate for each time interval i an estimate of the mean expected charge $\mu_i = \hat{n}_i(\vec{x}, t, \Delta t, \alpha) + r_{\mathrm{noise}}\Delta t$. In this sum $\hat{n}_i$ is the contribution due to the cascade α and $r_{\mathrm{noise}}\Delta t$ is a continuous noise contribution. In each time interval a counting experiment is performed, and the probability of a given measurement $\{n_i\}$ under the condition α can be calculated:

$$P(\{n_i\}|\alpha) = \prod_i \frac{\mu_i(\alpha)^{n_i}}{n_i!} \exp\left(-\mu_i(\alpha)\right). \qquad (1)$$

From this probability one can construct a maximum likelihood estimator, yielding the parameters $\hat{\alpha}$ best supported by the measurement:

$$\hat{\alpha} = \operatorname*{argmin}_\alpha \mathcal{L}(\alpha) \quad \text{where } \mathcal{L}(\alpha) = -\log P(\{n_i\}|\alpha). \quad (2)$$

The search for the global maximum in the seven-dimensional likelihood space is performed by minimizing the negative logarithm of the likelihood using the SIMPLEX minimizer in the MINUIT software package [43]. In order to avoid local minima the search is done iteratively, where in each step the minimizer starts at a different position in the parameter space. The iterative minimization and the many necessary table lookups for each time interval form a time-consuming procedure that cannot be applied to all events. However, this reconstruction finds the position of the particle shower with a resolution of 15 m horizontally and, due to the smaller DOM spacing, 5 m vertically. The energy resolution for an astrophysical neutrino spectrum is about 40% and the angular resolution is about 30°.

Other variants of the likelihood reconstruction described here have been developed and been used in more recent analyses. By incorporating improvements in the understanding of the detector response and a better modeling of the ice they provide better resolutions and determine IceCube's performance on cascades today [44].

V. EVENT SELECTION AND ANALYSIS METHOD

A small number of neutrino-generated showers need to be isolated from a large background of atmospheric muons. This is achieved by finding and applying a set of conditions on the reconstructed event properties that neutrino-induced showers fulfill, but atmospheric muons do not. In practice

this selection is implemented as a multistep process. The first steps in the process are aimed at conservatively reducing the background, allowing the use of computationally intensive reconstruction algorithms, that can be applied to a reduced set of events only. Each step in the event selection process is referred to as a "level." Level 1, the trigger condition, was described in Sec. II. Level 2, the online filter applied at the South Pole, and subsequent levels are outlined in this section. The section will first introduce the classification schemes and cut variables used for separation of the signal from the background and then turn to a description of the individual samples.

A. Background rejection methods and event property variables

The background rejection criteria used in neutrino cascade searches can be classified conceptually as belonging in the following four categories.

Reconstructed particle parameters.—Four different likelihood reconstruction routines are used in the searches described here. The routines differ in run time, precision, initial assumptions and in the number of neutrino parameters that they infer from the event. Three of the reconstruction routines return parameters with the hypothesis that the event is a particle shower. The fourth routine used assumes the event contains a muon track.

At earlier cut levels the CSCD_LLH likelihood reconstruction [45] is used. It does not account for the optical inhomogeneities of the ice but provides a quick estimate for the vertex and a quality parameter $\mathrm{rlogL_{cscd}}$ that describes how well the event fits to the cascade hypothesis.

Using the vertex estimate from CSCD_LLH another estimate for the deposited energy, E_{ACER}, is provided by the ATMCSCDENERGYRECO algorithm [46]. It is quick to compute and considers the optical inhomogeneities of the ice.

At later levels the CREDO algorithm described in Sec. IV provides the best estimates for the reconstructed vertex $\vec{x}_{\mathrm{CREDO}}^{(n)}$, deposited energy $E_{\mathrm{CREDO}}^{(n)}$ and zenith angle $\Theta_{\mathrm{CREDO}}^{(n)}$. The superscript (n) distinguishes, where necessary, applications of the CREDO algorithm with differing numbers of iterations.

All events are also reconstructed with another likelihood reconstruction [47] which assumes that the event contains a muon track. This routine gives a zenith angle estimate Θ_{track} and provides a quality of fit parameter $\mathrm{rlogL_{track}}$ for the track hypothesis. The zenith angle estimator correctly identifies much of the muon background as downgoing. Particle showers are preferentially interpreted as either horizontally or diagonally passing tracks which allows for some signal-background separation.

Containment and vetoing.—A particularly problematic background are muon events which pass close to the edges of the detector producing a light distribution which is similar to that produced by cascades. To counter this background various containment conditions are placed

on the position of the reconstructed vertex, the first-hit DOM and the DOM with the highest collected charge.

Events are excluded if the first-hit DOM or the DOM with the highest collected charge is located in the outermost vertical layer (see Fig. 2). Events are also vetoed if the depth of the first-hit DOM $z_{1^{st}}$ falls in the top or bottom 50 m of the detector.

The reconstructed vertex $\vec{x}_{CREDO}$ is required to lie inside the instrumented volume and not in the top or bottom 50 m of the detector. The analyses presented in this paper found different containment conditions on the xy position of the vertex to be optimal, when combined with their particular selection cuts, for suppressing background while maintaining signal efficiency. The two alternative containment conditions are illustrated by the solid and dashed lines in Fig. 2.

Topological characteristics.—The hit patterns of particle showers in IceCube are approximately spherical while the muon-track hit patterns are more elongated. A number of different quantities can be calculated to characterize the different topology of cascade and muon events and used to preferentially select cascades.

For example, a quantity analogous to the tensor of inertia of a rigid body is calculated for each event. The collected charge on each DOM takes the role of the rigid body's mass distribution. The ratio of the smallest eigenvalue to the sum of all of the eigenvalues, $\lambda = \lambda_{min}/\sum\lambda_i$, tends to $\frac{1}{3}$ for spherical events while muon tracks typically have smaller eigenvalue ratios [47].

Another way to select spherical events is to construct a spherical volume surrounding the reconstructed event vertex $\vec{x}_{CREDO}$ and consider the proportion of hit DOMs, versus the total number of DOMs, in this sphere. The radius of the sphere considered is chosen to scale with the average distance between reconstructed vertex $\vec{x}_{CREDO}$ and position of the hit DOMs—a robust estimate for the overall size of the hit pattern. The fill ratio f denotes the fraction of DOMs, falling within the sphere, on which light is recorded [40]. Hence, fill ratios close to 100% are obtained for spherical hit patterns, while muon events yield lower values. The fill ratio is especially efficient to suppress coincident muon events—two or more muons from different air showers that cross the IceCube detector within microseconds of each other. A second quantity, the difference Δf of two fill ratios with different radii, is also used. This quantity provides further separation power due to the fill ratio's dependency on the chosen radius being slightly different for the differently shaped hit patterns of cascades and tracks.

Time evolution and charge distribution.—Below PeV energies the Cherenkov light of particle showers originates within a few meters of the interaction vertex and then propagates through the detector with the speed of light in ice c_{ice}. In contrast, muon tracks traverse the detector with velocities close to the speed of light in vacuum c and emit Cherenkov photons continuously along their track. Several

approaches exploit this difference to separate cascade and track events.

A simple approach, that can be applied before the event vertex has been reconstructed, is the LINEFIT algorithm. The hit pattern is fitted with a straight line propagating with velocity v_{lf} [47]. Relativistic muons often yield LINEFIT velocities close to c whereas lower velocities are obtained if the fit is applied to cascades.

If the interaction time and vertex are well reconstructed, then causality can be used to provide a strong constraint on whether an event is a neutrino-induced particle shower event. For each DOM, light is expected to arrive at the earliest after the time necessary to cover the distance between the DOM and the vertex, at velocity c_{ice}. While delayed photon arrivals are common due to light scattering in the ice, much earlier arrival times indicate a problem with the cascade hypothesis. The difference between the expected ($t_{expected}$) and observed (t_{hit}) arrival time is calculated for all DOMs and Δt_{min} is defined as the smallest such delay time $\Delta t_{min} = \min(t_{hit} - t_{expected})$. Events with large negative values of Δt_{min} are removed.

Another approach is to sort the DOMs by the time they recorded light and then consider the unit vector from one hit DOM to a subsequent hit DOM as an individual dipole moment. The global dipole moment m is obtained by averaging over all individual dipole moments. Larger moments are expected from tracks and smaller moments from cascades [47].

Yet another way to emphasize the different hit pattern evolution of tracks and cascades is to divide the event into two parts based on the times of the hit DOMs. This splits tracks into two disjunct segments and cascades into two mostly concentric shells. The CSCD_LLH algorithm is used to obtain, for each half, the vertices $\vec{x}_1$ and $\vec{x}_2$. Large radial and vertical distances Δr_{12} and Δz_{12} between the vertices as well as large differences in the reconstructed time Δt_{12} are then indicative of tracks.

Another feature of cascade events, which is also related to the fact that the particle showers are only a few meters in length, is that most of the light is recorded close to the vertex and hence early in the event. In contrast, since muons emit light continuously along their track it is more likely to see later contributions to the total charge. The variable $\Delta t_{50\%-90\%}$ denotes the fraction of the event length in which the total collected charge rises from 50% to 90%. Greater $\Delta t_{50\%-90\%}$ values indicate a longer time interval for the second half of the event's total charge to be collected and are more likely to occur for muon events.

Some discrimination power comes from DOMs where just enough light arrives to trigger the readout and hence only a single pulse is reconstructed from the waveform. A combination of light yield, scattering in the ice and the geometric shape of the hit pattern results in a slightly higher number of these DOMs for muons. The ratio n_1/n_{hit} of DOMs with only one reconstructed pulse over the

total number of hit DOMs tends to smaller values for cascades.

Finally, a useful variable is the ratio of the charge collected in the DOM with the highest charge, compared to the total recorded charge q_{max}/q_{tot}. Low energetic muons passing very close to one DOM can yield a high charge concentration in this DOM compared to others. These events can resemble cascadelike hit patterns and are prone to be overestimated in energy. Hence, requiring a low ratio q_{max}/q_{tot} is useful to reject this class of background events.

B. Analysis overview

Three event selections were developed to search for neutrinos in the IceCube-40 data set. In the order of their energy thresholds they are labeled Ia, II and Ib. The multiple event selections allowed sensitivity to both high-energy astrophysical and low-energy atmospheric neutrinos as well as providing a collaboration internal cross-check.

The different event selections rely on similar selection methods that are differently combined for the individual goals of the analyses. The event selections share the first three filter levels but differ at later filter steps, since analysis Ia aimed at measuring atmospheric neutrinos whereas analyses Ib and II were optimized towards an astrophysical neutrino flux. In order to avoid experimenter bias a blind analysis was performed. Each event selection was developed and tested on simulation and a 10% subset of the experimental data, sampled uniformly over the year. A simple cut-and-count experiment was done on the remaining 90%.

Analyses Ia and Ib were developed in parallel to analysis II, but only unblinded afterwards. The crucial difference is that they utilized a significantly improved background simulation described in Sec. III, resulting in the choice of tighter cuts and a purer neutrino sample. Consequently here

the focus is put on samples Ia and Ib. An overview of the cuts performed to obtain the three samples is given in Table I. A comparison of the energy thresholds and event rates is given in Table IV.

Sizable systematic uncertainties must be considered in interpreting the result. Therefore for samples Ia and Ib a Bayesian approach was chosen (described in the Appendix) and the result is reported in form of the posterior probability for the number of nonbackground events.

C. Filter level 2 and 3

Triggered events are filtered online at the South Pole to reduce the data volume to the bandwidth available for data transfer from the Pole via satellite. The online filter, or level 2, is a filter on easy-to-compute variables that retains the majority of the neutrino signal while removing a large fraction of the background. It requires the LINEFIT velocity to be $v_{lf} < 0.13$ m/ns and the tensor-of-inertia eigenvalue ratio to be $\lambda > 0.12$. The distributions of these variables are shown in Figs. 5(a) and 5(b). At this early stage of the event selection, where no event quality cuts are done yet, the distributions show some disagreement between data and simulation. Further steps in the event selection will reduce this disagreement, mostly by removing events that are too low in energy or that are not contained in the instrumented volume. The pole filter reduced the data rate by 2 orders of magnitude to approximately 16 Hz.

Because of the energy threshold of about 100 GeV and the steeply falling energy spectrum, the energy distribution of background events passing level 2 is strongly peaked at lower energies. As the majority of the events are still atmospheric muons most of the events are reconstructed as downgoing tracks [see Fig. 6(a)]. Consequently, the level 3 cuts concentrate on reducing the background at low energies.

TABLE I. Comparison of the event selections. The symbols used here are described in Sec. V A.

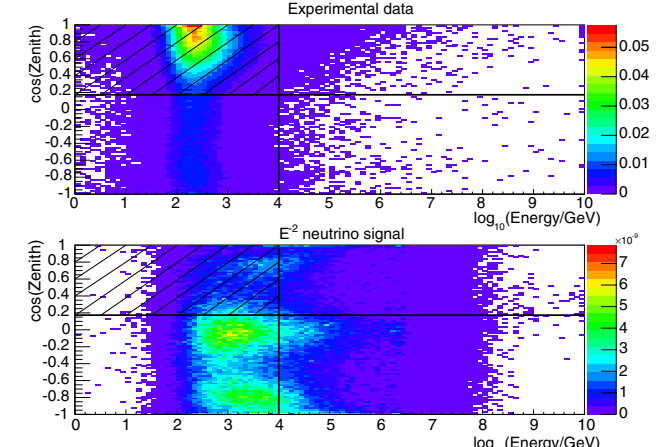|	Atmospheric neutrinos	Astrophysical neutrinos	
Optimized for	Sample Ia	Sample Ib	Sample II
Level 1	light recorded on 8 different DOMs within a 5 μs time window		
Level 2	$v_{lf} < 0.13$ m/ns, $\lambda > 0.12$		
Level 3	$(E_{ACER} > 10$ TeV$)$ or $(E_{ACER} < 10$ TeV, $\Theta_{track} > 80°$, rlogL$_{cscd} < 10)$		
Level 4	$N_{strings} > 5$, -450 m $< z_{1^{st}} < +450$ m, DOM with first hit not on outer string		$E_{CREDO}^{(1)} > 2.5$ TeV, $\Delta r_{12} < 40$ m, $f > 0.4$
Level 5/6	DOM with largest charge not on outer string, $\vec{x}_{CREDO}^{(8)}$ contained, -500 m $< z_{CREDO}^{(8)} < +500$ m, $E_{CREDO}^{(8)} > 1.8$ TeV, $\Delta t_{min} > -75$ ns, $q_{max}/q_{total} < 0.3$, $f > 0.6$		DOM with largest charge not on outer string, $\vec{x}_{CREDO}^{(4)}$ contained, -450 m $< z_{CREDO}^{(4)} < +450$ m
BDT input	rlogL$_{cscd}$, Δr_{12}, Δz_{12}, n_1/n_{hit}, $\Delta t_{50\%-90\%}$, Δt_{min}, $\cos(\Theta_{CREDO}^{(8)})$, $\cos(\Theta_{track})$, Δf, λ, m		$z_{CREDO}^{(4)}$, Θ_{track}, rlogL$_{track}$, v_{lf}, λ, f, Δt_{12}, $|\vec{x}_1|$
Final cuts	BDT$_I > 0.5$	BDT$_I > 0.1$ $E_{CREDO}^{(8)} > 100$ TeV	BDT$_{II} > 0.2$, $E_{CREDO}^{(4)} > 25$ TeV
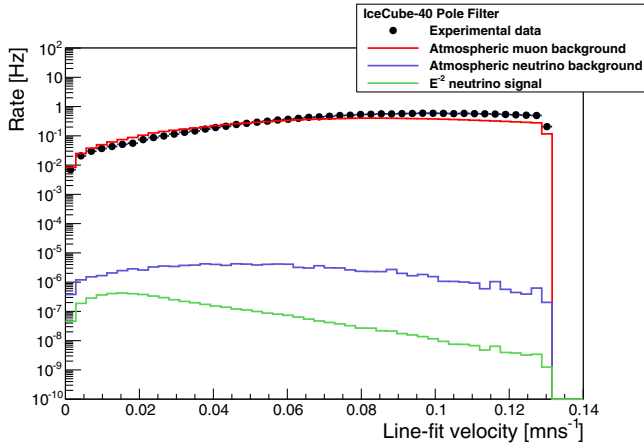
(a)
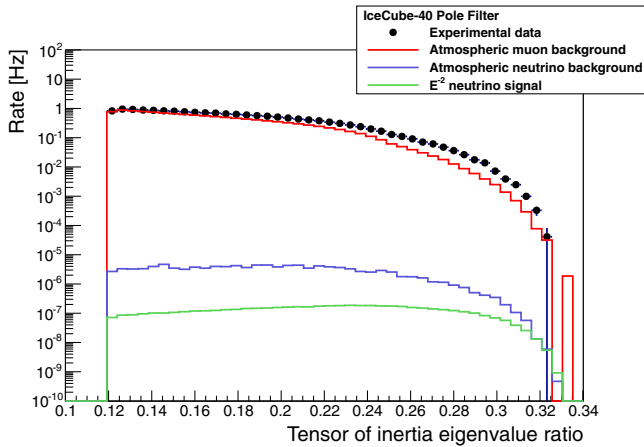
(b)

FIG. 5 (color online). The IceCube-40 online filter, the data are shown by the black filled circles, simulated atmospheric muon background by the red line, simulated atmospheric electron neutrinos by the blue line, and simulated electron neutrino signal with spectrum $E^2 dN/dE = 3.6 \times 10^{-8}$ GeV sr^{-1} s^{-1} cm^{-2} by the green line.

(a)

(b)

FIG. 6 (color online). The IceCube-40 level 3 filter variables. (a) The level 3 zenith angle and energy reconstructions. The two panels show the data and E^{-2} spectrum electron neutrino signal. The level 3 cuts are represented by the black lines at zenith $\Theta_{track} = 80°$ and energy $E_{ACER} = 10$ TeV. Events in the hatched upper left quadrant of each of the panels were removed. (b) The reduced log-likelihood rlogL_{CSCD}. The data are shown by the black filled circles, simulated atmospheric muon background by the red line, simulated atmospheric electron neutrinos by the blue line, and simulated electron neutrino signal with spectrum $E^2 dN/dE = 3.6 \times 10^{-8}$ GeV sr^{-1} s^{-1} cm^{-2} by the green line. Events with rlog$L_{CSCD} < 10$ were removed.
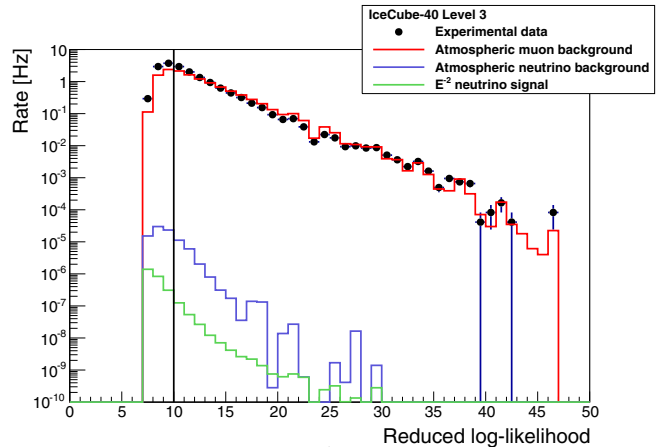
All events with a reconstructed energy $E_{ACER} > 10$ TeV are kept, whereas lower energetic events are subject to two more cuts. First, when reconstructed under a muon track hypothesis, events reconstructed as downgoing with zenith angles $\Theta_{track} < 80°$ are rejected. Secondly, those events are removed, where a CSCD_LLH likelihood value of rlog$L_{cscd} > 10$ indicates a poorly fitted event. After application of the level 3 filter the data rate is reduced by another order of magnitude to approximately 1.8 Hz, while contained astrophysical (atmospheric) neutrinos were kept with an efficiency of 76.5% (56.6%).

D. Sample Ia

After level 3, the analyses diverge. Event selection Ia aims at the observation of atmospheric neutrinos with energies of a few TeV. Previous cuts aimed to provide

an optimal efficiency for cascades regardless of their energy and position inside the detector. As a consequence at level 3 a significant number of events, that are very low in energy or happening at the border of the instrumented volume, remain in the sample. For these events no reliable separation between signal and background could be found.

Therefore, a set of geometric conditions has been defined to remove such events: it is required that the first-hit DOM is neither on the outer layer of IceCube-40 (red squares in Fig. 2) nor in the top or bottom 50 m of the detector. Also DOMs on at least five different strings must have recorded

light. This cut reduces the data rate to 79 mHz, while contained astrophysical (atmospheric) neutrinos are kept with an efficiency of 56.1% (37.2%).

After these cuts, at the so-called level 5, additional reconstructions but no cuts were performed. In particular the remaining sample was small enough to perform the CREDO likelihood reconstruction described in Sec. IV with eight iterations. Muon background still dominates over atmospheric neutrino-induced showers by 3 orders of magnitude at selection level 5. Therefore, the vertex and energy estimates are used to apply another series of event selection conditions.

At level 6, the energy threshold is set to $E^{(8)}_{\mathrm{CREDO}} > 1.8$ TeV. In order to remove events where low energetic muons pass very close to a DOM and where their energy is likely to be overestimated, a cut on $q_{\mathrm{max}}/q_{\mathrm{tot}} < 0.3$ is applied. Furthermore, the containment requirement is enforced: the reconstructed vertex must lie inside the blue solid boundary shown in Fig. 2, its z coordinate must be inside the instrumented depth interval and also the DOM with the highest recorded charge in the event may not be on the outer layer. A constraint on the minimum delay time $\Delta t_{\mathrm{min}} > -75$ ns is used to remove events where causality rules out the cascade hypothesis. Together with requiring a fill ratio $f > 0.6$, this set of cuts reduces the data rate by 2 orders of magnitude down to 660 μHz, while retaining efficiencies for contained

astrophysical and atmospheric neutrinos of 66.4% and 20.1%, respectively. Overall agreement of event properties between simulation and experimental data is good (see Fig. 7). This is a necessary precondition for the final event selection step, which uses a multivariate algorithm to distinguish signal and background events.

The final step of the event selection is to remove the remaining background and obtain a sample dominated by neutrinos. For this purpose event properties that still provide separation power are used as input to a multivariate algorithm to obtain a single quality parameter for each event. The TMVA package [48] is used to train a boosted decision tree (BDT). In total 11 variables are combined into one final event quality variable $\mathrm{BDT}_{\mathrm{I}}$. These are the CSCD_LLH algorithm's quality parameter $\mathrm{rlogL}_{\mathrm{cscd}}$, the vertical and radial distances Δz_{12}, Δr_{12} of the time-split reconstructions, the fraction of DOMs with only one reconstructed pulse n_1/n_{hit} and the fraction of the event duration needed to accumulate the second half of the total charge $\Delta t_{50\%-90\%}$. The two zenith angle estimators $\Theta^{(8)}_{\mathrm{CREDO}}$ and Θ_{track} enter the BDT as well as the dipole moment m and the fill-ratio difference for two radii Δf. Finally, the eigenvalue ratio λ and the minimum delay time Δt_{min} are used, too. They have already been used at earlier cut levels but still provide some discrimination power. The four variables ranked most important by the classifier are shown in Fig. 7.
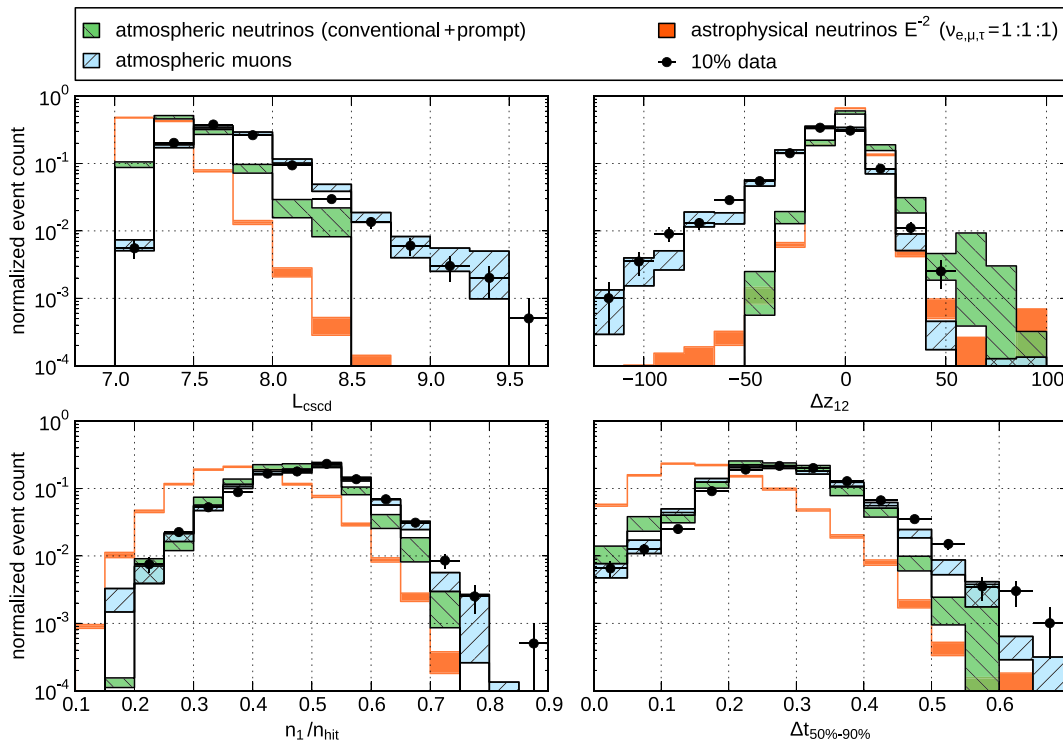

FIG. 7 (color online).   At level 6, 11 input variables are combined to train a boosted decision tree. Individually the variables provide only limited separation power, especially for distinguishing atmospheric neutrinos and muons. The four most important variables according to the classifier are shown here at level 6. Definitions of the variables can be found in Sec. V A. The shaded regions in the plot denote the statistical uncertainties.
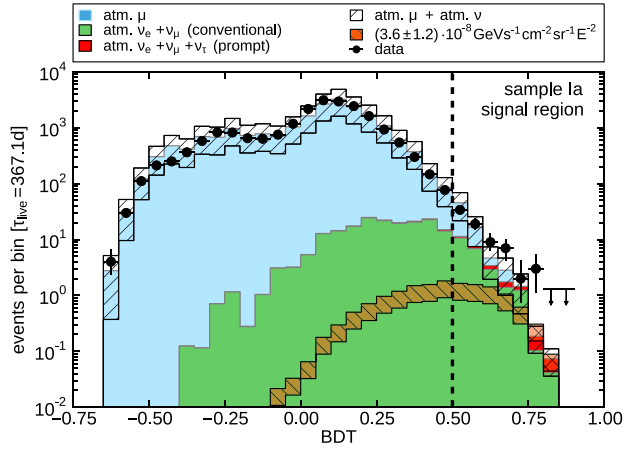
FIG. 8 (color online).   The BDT output variable at Level 6. A cut at $BDT_I > 0.5$ defines the sample Ia. The atmospheric muon and neutrino components are stacked on top of each other and describe together the recorded data well. The experimental data shown comprise 100% of the sample. For bins in which no event was observed a 68% C.L. upper limit is shown. The white hatched area shows the distribution of atmospheric muons and neutrinos, including systematic and statistical uncertainties. The orange hatched area denotes the prediction of astrophysical neutrinos according to the flux estimate from [11].

The distribution of the BDT output variable and its ability to separate signal from background is shown in Fig. 8. At low values, the distribution is dominated by the atmospheric muon background and the experimental data are adequately described by the CORSIKA simulation. The signal distribution centers at higher BDT scores, but even there a contribution from atmospheric muons is present. Closer inspection reveals that these events are muons with prominent bremsstrahlung cascades and little to no hint of the muon track. The events resemble neutrino-induced particle showers rather well. The geometry of IceCube-40 with one dimension being much shorter than the others is obviously vulnerable to this class of background events. In the energy range below 100 TeV, with the given detector and the aforementioned background rejection methods, including their combination within a multivariate classifier, these events turn out to be irreducible background.

This limits the possible background suppression for sample Ia. Atmospheric neutrino signal and muon background are similarly distributed at BDT_I scores > 0.5, so cutting at a higher value removes the atmospheric neutrino signal as much as the atmospheric muon background. As a consequence a BDT_I value of 0.5 is the optimal separation point between background and signal that maximizes the detection potential [49] for an atmospheric neutrino flux. However, a rather large number of 71 events is expected in sample Ia from which 41 are expected to be atmospheric muons and 30 conventional and prompt neutrinos. Both numbers are affected by rather large systematic uncertainties, which are discussed in Sec. VI.

E. Sample Ib

The remaining background events can be removed by increasing the energy threshold of the analysis. Because of their steeply falling spectrum conventional atmospheric neutrinos are severely reduced by an energy cut. However, the harder spectra of prompt neutrinos and the assumed diffuse astrophysical neutrino flux are not so much affected. This fact is used to define the data sample Ib with an energy threshold of $E_{CREDO}^{(8)} > 100$ TeV. A comparatively loose requirement on the BDT score of $BDT_I > 0.1$ is then sufficient to remove all simulated background events (see Fig. 9). In contrast to sample Ia, which was designed to find atmospheric neutrinos, sample Ib has a significantly better performance for detecting a prompt or astrophysical neutrino flux.

For this sample, the background contribution from atmospheric muons cannot be determined from simulation anymore as all events have been removed. In order to estimate the muon rate, the reconstructed energy distribution is extrapolated from the low-energy region, where simulated events are still available, to higher energies.

Up to PeV energies, the energy spectrum of the brightest bremsstrahlung cascades along simulated muon tracks can be described by a power law $dN/dE \propto E^{-3.7}$. For muon events, which pass the event selection, the corresponding energy spectrum is not necessarily the same, because of the energy-dependent performance of the cuts. For
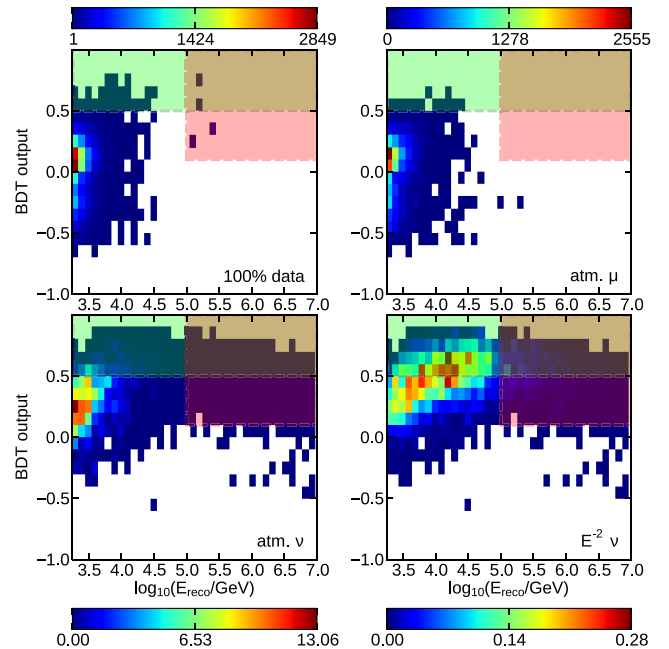

FIG. 9 (color online).   The parameter space spanned by the BDT output variable and the reconstructed energy. The green shaded area ($BDT_I > 0.5$) and the red shaded area ($BDT_I > 0.1$)& ($\log_{10}(E_{reco}/GeV) > 5$) denote the cuts of samples Ia and Ib, respectively. The color scale denotes linearly the expected/seen number of events per bin in 100% of the live time.
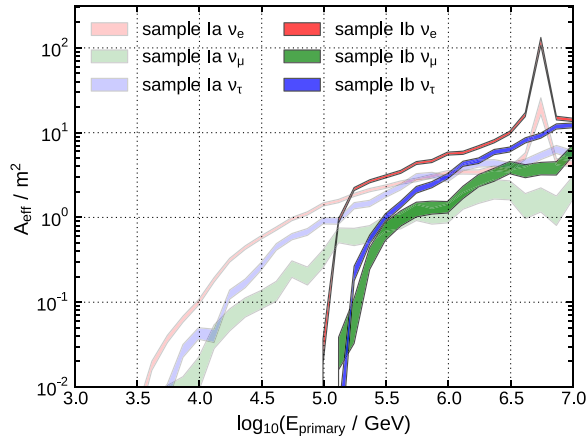
FIG. 10 (color online). Effective areas for different neutrino flavors in samples Ia and Ib.

example, muon events with bright bremsstrahlung cascades are suppressed with increasing energy, since the muon becomes more likely to be detected in the veto region. On the other hand, the selection efficiency for particle showers rises with increasing deposited energy. Hence, the model used to extrapolate the muon background into the signal region is the product of two functions: the selection efficiency for particle showers as a function of deposited energy (derived from simulation) and a power law with the index and normalization as free parameters.

This model provides a reasonable fit to the energy distribution of background muons below the energy threshold [see Fig. 11(b), the same BDT_I score > 0.1 is required for these events as for the events in the high-energy sample]. The fit is consistent with the expectation that the remaining background events are dominated by high bremsstrahlung cascades and that the energy estimator describes their energy spectrum. This confirms the physical motivation of the extrapolation in the signal region. From the extrapolation one can amount the muon contribution to $0.04^{+0.06}_{-0.02}$ events, where the errors are derived from varying the parameters within the uncertainties obtained from the fit. An additional 0.21 events are expected from conventional and prompt atmospheric neutrinos.

This event selection reduced the muon background by 7 orders of magnitude from the rate after the online filter. This high suppression comes at the price of a low total efficiency of 5% (0.5%) for contained astrophysical (atmospheric) neutrinos. The energy-dependent selection efficiencies are presented in the form of effective areas for both samples in Fig. 10. Table II summarizes the performance of the event selection at different cut levels.

F. Sample II

Level 4 for the event selection sample II enforces a moderate energy cut of $E^{(1)}_{CREDO} > 2.5$ TeV and selection for cascadelike events using two of the topological
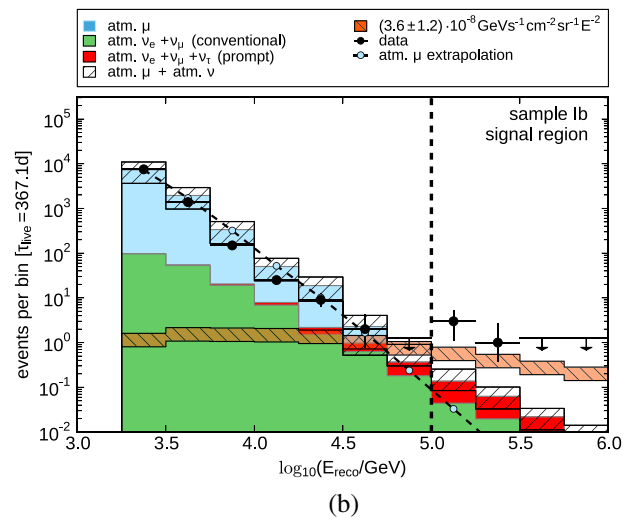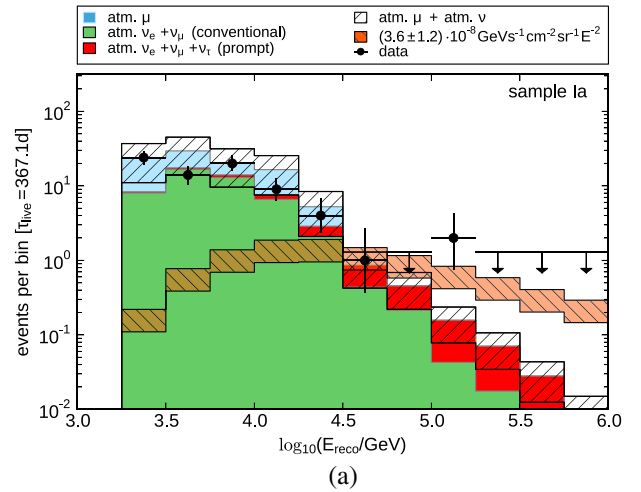

FIG. 11 (color online). The reconstructed energy distributions for samples Ia (a) and Ib (b). The atmospheric muon and neutrino components are stacked on top of each other. The experimental data shown comprise 100% of the sample. For bins in which no event was observed a 68% C.L. upper limit is shown. The white hatched area shows the distribution of atmospheric muons and neutrinos, including systematic and statistical uncertainties. The orange hatched area denotes the prediction of astrophysical neutrinos according to the flux estimate from [11]. (a) Deposited Energy in sample Ia. (b) Deposited Energy in sample Ib. The plot extends into the background region below 10^5 GeV. From there the contribution of atmospheric muons is extrapolated to higher energies (black dashed line).

variables described in Sec. V A. The difference between the split vertex reconstruction is restricted to ($\Delta r_{12} < 40$ m) and high fill ratios ($f > 0.4$) are required. The CREDO reconstruction is performed with four iterations on the remaining events to increase the accuracy of the vertex and energy estimate. The next set of cuts focus on selecting contained events. The xy coordinates of $\vec{x}^{(4)}_{CREDO}$ must lie inside the area circumscribed by the blue

TABLE II. Event rates and cut efficiencies at the different levels leading to samples Ia and Ib. While the data column refers to all recorded events that pass the cuts, the neutrino rates refer to contained events, i.e. neutrinos which have their interaction vertex inside the area circumscribed by the blue solid line in Fig. 2. For charged current ν_μ interactions the muon must have its highest energy loss inside the area.

| | | Contained neutrinos | |
| | Experimental | | HKKMS07 |
Cut level	data	$3.6 \times 10^{-8} E^{-2}$	(no knee)
		Rates in μHz	
Level 2	16.03×10^6	1.28 ± 0.03	153 ± 4
Level 3	1.74×10^6	0.97 ± 0.01	86 ± 1
Level 4/5	78980	0.550 ± 0.008	32.1 ± 0.7
Level 6	660	0.365 ± 0.006	6.5 ± 0.3
Sample Ia	2.34	0.156 ± 0.004	0.73 ± 0.08
Sample Ib	0.105	0.068 ± 0.001	0.0021 ± 0.0003
		Efficiencies with respect to previous level	
Level 3	10.8%	76.5%	56.6%
Level 4/5	4.5%	56.1%	37.2%
Level 6	0.8%	66.4%	20.1%
Sample Ia	0.4%	42.8%	11.3%
Sample Ib	0.02%	18.6%	0.04%

dashed line in Fig. 2 and the z coordinate must lie between ± 450 m. The DOM with the highest charge is not allowed to be on the veto layer of strings.

As in samples Ia and Ib, a boosted decision tree is trained to combine the variables, which still have discrimination power, into one event quality parameter BDT_{II}. Eight variables are used: the zenith angle Θ_{track} and fit quality parameter $rlogL_{track}$ of the track reconstruction; the online filter variables v_{lf} and λ; the fill ratio f and the vertex time difference Δt_{12}. Information on where in the detector the event occurred entered the BDT in the form of the z coordinate of $\vec{x}^{(4)}_{CREDO}$ and the distance of $\vec{x}_1$ to the detector center. A cut at $BDT_{II} > 0.2$ and $E^{(4)}_{CREDO} > 25$ TeV is found to be optimal to select astrophysical neutrinos.

The event selection criteria for sample II were finalized before those of samples Ia and Ib. The available statistics of simulated background events were limited and did not describe the data particularly well due to a lack of high-energy proton-induced air showers. Hence, unlike for samples Ia and Ib, the full simulation discussed in Sec. III did not enter the optimization of the event selection. Instead, when training the BDT, experimental data were used for the background sample. The final energy threshold was set to 25 TeV, which—given the limited background simulation available at that time—leads to an optimal sensitivity for an astrophysical E^{-2} flux. The final numbers presented here for the background estimate are based on the full statistics. Further information about the event selection can be found in [50].

VI. SYSTEMATIC UNCERTAINTIES

The three event samples (Ia, Ib, II) share common sources of systematic uncertainties. The largest uncertainties on

the expected event count arise from our limited knowledge of the optical ice properties at the South Pole, the selection efficiency of the muon background and the theoretical predictions for the atmospheric neutrino flux. Table III summarizes the systematic uncertainties for sample Ia and Ib. The systematic uncertainties associated with sample II are similar to those of sample Ib. The individual systematic errors are described in more detail below.

In calibration runs, where LEDs inside the DOMs illuminate the detector, data are obtained from which the characteristics of the light absorption and scattering at different points throughout the ice can be estimated. The estimated characteristics form a so-called ice model which contains the depth, wavelength, and temperature-dependent optical properties throughout the detector and the surrounding ice and bedrock. The AHA ice model [51] was used in all simulations for this analysis. To carry out a study of the uncertainties arising from the ice model, simulated data sets were produced using an alternative ice model, called SPICE [52] which was developed after this analysis was complete. The systematic uncertainty on the event rate due to the ice model was estimated to be $\pm 24\%$ for an E^{-2} neutrino spectrum signal and $\pm 11\%$ for the atmospheric neutrino background for the three samples Ia, Ib and II.

The estimate of the rate of atmospheric muons that pass the selection cuts is also affected by a rather large uncertainty. The simulation falls short in providing an absolute rate estimate, by systematically underestimating the measured muon rate. At cut levels before level 6, where the data-to-simulation agreement is not yet optimal, cuts affect data and simulation events slightly differently. Hence, the rate discrepancy changes slightly between cut levels. At each of these levels the rate estimate from atmospheric muon simulation can be normalized to match

TABLE III. Overview on systematics uncertainties on the event count for analyses Ia and Ib. The systematic uncertainties associated with sample II are similar to those of sample Ib except for the atmospheric muon prediction. Unlike sample Ib both samples Ia and II estimate the muon background from simulation for which similar systematic uncertainties apply. See Sec. VI for further details.

| | Sample Ia (low energies) | | Sample Ib (high energies) | |
	Atm. ν	$E^{-2}\nu$	Atm. ν	$E^{-2}\nu$
DOM efficiency	14%	4%	17%	4%
Ice model	24%	11%	24%	11%
ν cross sections	3%	6%	3%	6%
Theoretical	$-26\% + 25\%$	n/a	$-37\% + 27\%$	n/a
Neutrino knee	$-16\% + 0\%$	n/a	$-23\% + 4\%$	n/a
Total	$-41\% + 37\%$	13%	$-50\% + 40\%$	13%
	Atm. μ (simulated)		Atm. μ (extrapolated)	
Total	50%		$-50\% + 150\%$	

the measured data rate by applying factors of 1.25–2. As described in Sec. V, the event selection for samples Ia and Ib removes problematic event classes and creates a sample with good data-to-simulation agreement before training the boosted decision tree. At that point the normalization factor is 1.54 and is fixed for the rest of the analysis. The observed $\pm 50\%$ variation of this normalization factor at early cut levels is used as an estimate for the total systematic uncertainty on the muon rate for samples Ia and II, since both estimate the atmospheric muon background from simulation. The variation encompasses uncertainties on the cosmic-ray spectrum and composition, the particle interactions within air showers, the DOM efficiencies (see below) and the optical properties of the ice. About 10% of it can be attributed to the uncertainty of the cosmic-ray energy spectrum. This value is obtained by varying the broken power law parameters in the range of their published uncertainties [38]. Optimally, the other uncertainties would be quantified by varying the respective parameters in the simulation. However, the generation of several additional sufficiently sized background samples is computationally intractable and we are hence left with the empirical estimate of 50% uncertainty for the atmospheric muon background.

For sample Ib the atmospheric muon background is estimated not from simulation but from a fit of the reconstructed energy distribution and its extrapolation to higher energies. From varying the fitted parameters within the uncertainties reported by the fit, the systematic uncertainty of the muon rate in sample Ib is estimated to be $(-50\%, +150\%)$. Although this percentage uncertainty is larger than for samples Ia and II, the background contribution of atmospheric muons in sample Ib is much smaller than the contribution from atmospheric neutrinos. Consequently in sample Ib the total systematic uncertainty of the combined background is dominated by atmospheric neutrinos. This is not the case for samples Ia and II.

A DOM's efficiency is the ratio of the light collected by a DOM to the total light incident upon that DOM. The DOM efficiency includes the quantum efficiency of the PMT and the transmissivity of the optical gel and glass of each sphere. A $\pm 10\%$ uncertainty in DOM efficiency is estimated for IceCube DOMs [21]. By changing the DOM efficiency in the simulation the effect on astrophysical (atmospheric) neutrinos event rates can be quantified to $\pm 4\%$ ($\pm 14\%$) for sample Ia and $\pm 4\%$ ($\pm 17\%$) for samples Ib and II.

The simulation for this analysis assumed neutrino-nucleon cross sections based on CTEQ5 parton distribution functions (PDFs)[53]. The updated CSS [54] calculation using the ZEUS global PDF fit predicts smaller cross sections. By comparing simulated neutrino data sets with both models the systematic uncertainty from the neutrino cross-section model is quantified as $\pm 6\%$ ($\pm 3\%$) for astrophysical (atmospheric) neutrinos.

The uncertainty in the atmospheric neutrino flux prediction has two components: the theoretical uncertainty from the original calculations and the uncertainty in modifying the HKKMS07 model to include the atmospheric neutrino knee. The theoretical uncertainty of the conventional neutrino flux in the HKKMS07 model is about 25% [25]. Since the ERS model is used as a baseline for the prompt component its uncertainties are adopted [26]. Combined, these result in a systematic uncertainty of the atmospheric neutrino flux of $(-26\%, +25\%)$ and $(-37\%, 27\%)$ in samples Ia and Ib, respectively. For sample II we conservatively assume the uncertainty from the high-energy sample Ib. The knee in the cosmic-ray spectrum should lead to a similar feature in the atmospheric neutrino spectrum. The effect depends on the respective model for the cosmic-ray spectrum and the energy transfer from the primary to the neutrino. Because of the different energy ranges the samples are affected differently. The uncertainty was quantified to be $(-16\%, +0\%)$ for sample Ia and $(-23\%, +4\%)$ for sample Ib. For sample II we adopt the larger values of the high-energy sample Ib.

Table III shows the resulting systematic uncertainty for the various samples, where the total uncertainties are obtained from adding each systematic uncertainty in quadrature.

VII. RESULTS AND DISCUSSION

We have prepared three different event selections of cascadelike events, each aiming at somewhat different energies. In the following, we discuss the results starting with Ia, the analysis with the lowest energy threshold, and then move up in energy to II and Ib. The reported results refer to 90% of the experimental data, which were kept blind during the development of the event selections. A summary of the results from the three analyses is presented in Table IV.

Sample Ia with an energy threshold of about 2 TeV aimed at the observation of atmospheric neutrinos, which for this sample will be called the signal. In total 67 events were observed over an expectation of 41.1 events from atmospheric muons and 27.8 from conventional and 2.25 prompt atmospheric neutrinos, respectively. Accordingly, the excess above atmospheric muons is quantitatively well described by the atmospheric neutrino prediction by the HKKMS07 and ERS models. The rather large uncertainty of the atmospheric muon background requires a careful evaluation of the significance of the atmospheric neutrino excess. We marginalize over the uncertainty in background and signal prediction using the method described in the Appendix. The 90% credible interval ranges from 5 to 62 nonbackground events, or 16% to 206% of the predicted conventional and prompt neutrino flux. The significance of the excess over atmospheric muons including systematic errors is 1.1σ. No observation of atmospheric neutrinos is claimed. The average event energies of atmospheric neutrinos are 6 TeV and hence comparable to the highest energy bin of the completed analyses of contained events inside the DeepCore/IceCube 79-string configuration [13].

In sample II with an energy threshold of about 25 TeV we observed 14 events after event selection, on an expected background of 3.0 atmospheric neutrino events and 7.7 atmospheric muon events. As the analyses was optimized for highest sensitivity towards a diffuse E^{-2} spectrum—harder than the spectrum of atmospheric neutrino and

muon events—the analysis has a higher energy threshold. However, it was only realized after unblinding that protons were underrepresented at high energies in the simulation of the cosmic-ray spectrum (see Sec. III), leading to an underrepresentation of the muon background and suboptimal loose final cuts. As a result, the purity of the sample is only comparable to that of sample Ia. A small and insignificant excess of events is observed over the background of atmospheric neutrinos and muons. We calculate an all-flavor flux limit [49] using the TRolke method [55] to include systematic errors. For an E^{-2} astrophysical neutrino spectrum and assuming a $1:1:1$ flavor ratio at the Earth, the all-flavor flux limit at a 90% confidence level is

$$E^2\Phi_{\text{lim}} \le 7.46 \times 10^{-8} \text{ GeV sr}^{-1} \text{ s}^{-1} \text{ cm}^{-2}. \quad (3)$$

The energy range for this calculation containing 90% of the signal is from 25 TeV to 5 PeV.

Sample Ib, with an energy threshold of 100 TeV, is the high-energy counterpart of sample Ia, differing only in the lower BDT cut and higher energy cut. The cuts were optimized for highest sensitivity towards an E^{-2} spectrum and the tighter cuts lead to a purer neutrino sample. In total three events were found over an expectation of 0.04 from atmospheric muons and 0.21 from atmospheric conventional and prompt neutrinos. At these higher energies the expected contribution from prompt neutrinos exceeds the conventional neutrinos by a factor of 3. The events have energies of 144 ± 60, 144 ± 60 and 224 ± 90 TeV. One additional event with 135 ± 50 TeV was also in the 10% sample used to develop the analysis. It is not considered in the significance calculation. Images illustrating the hit pattern of all four events are shown in Fig. 12.

The three events found are a rather large excess, not only above the muonic background but also above the atmospheric neutrinos. It corresponds to 2.7σ above both classes of background. We have employed the method described in the Appendix allowing us the inclusion of all systematic and statistical errors on the background

TABLE IV. Event count predictions and results for the different samples and for models of conventional, prompt and astrophysical neutrinos. The model predictions are calculated for 90% of the experimental data. Where they are derived from simulation the statistical errors are given. The three lines of the ERS model show the uncertainty band.

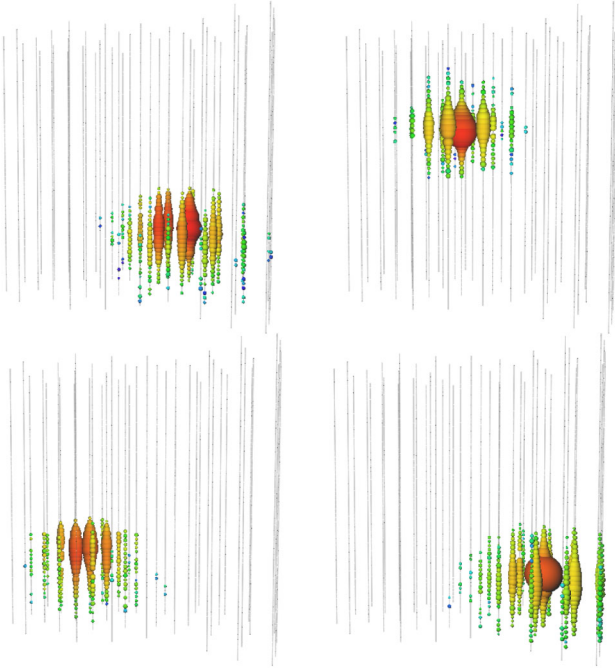| Sample	Ia	II	Ib
E_{cut}	2 TeV	25 TeV	100 TeV
10% sample	7	2	1
90% sample	67	12	3
Atm. μ	41.1 ± 9.5	7.7 ± 1.8	0.04
Bartol (no knee) [29]	25.5 ± 2.8	2.12 ± 0.2	0.078 ± 0.012
HKKMS07 (+knee) [25,27,28]	27.8 ± 3.0	1.68 ± 0.16	0.054 ± 0.009
ERS [26] (max.)	2.76 ± 0.07	1.21 ± 0.03	0.198 ± 0.005
ERS [26]	2.25 ± 0.06	0.95 ± 0.02	0.155 ± 0.004
ERS [26] (min.)	1.29 ± 0.03	0.57 ± 0.01	0.090 ± 0.002
Martin GBW [56]	1.14 ± 0.03	0.48 ± 0.01	0.078 ± 0.002
$3.6 \times 10^{-8} E^{-2}$	4.54 ± 0.12	4.93 ± 0.12	1.96 ± 0.05

FIG. 12 (color online). Three cascadelike events above 100 TeV were found in samples II and Ib. An additional event was already found in the 10% sample used to develop the cuts. The event displays visualize the light distribution in the detector: Each DOM is shown as a sphere, which size scales with the recorded charge by the DOM. The color coding illustrates the arrival time of the light at the DOM ranging from red (early hits) over green to blue (late hits).
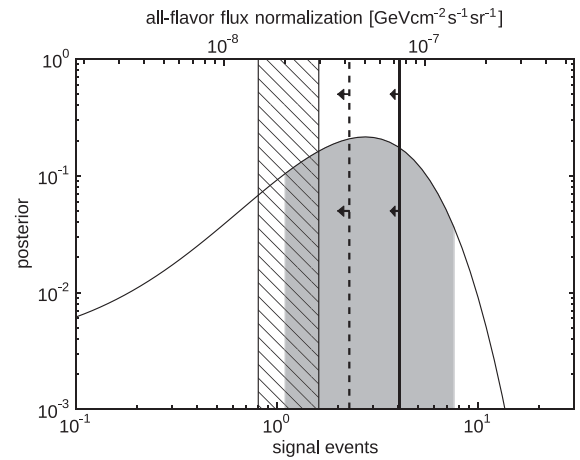

FIG. 13. Posterior probability for additional signal events in sample Ib. The gray shaded area shows the 90% credible interval of this work and the hatched area denotes the expected number of events according to the best fit flux in [11], including a cutoff at 2 PeV. The solid and dashed lines show the 90% C.L. upper limits derived from sample II and the IceCube-59 diffuse muon search [28], respectively. The upper x axis transforms an expected event count into an all-flavor flux normalization of an unbroken E^{-2} power law. In transforming the flux estimate and cutoff from [11] to an unbroken power law, a slightly lower flux normalization is obtained.

expectation to calculate the posterior probability for the potential signal flux shown in Fig. 13. As a consequence of the observed excess the posterior peaks around a flux normalization for an unbroken all-flavor E^{-2} flux of $5 \times 10^{-8} \text{ GeV sr}^{-1} \text{ s}^{-1} \text{ cm}^{-2}$. The 90% credible interval covers the range $(2\text{--}14) \times 10^{-8} \text{ GeV sr}^{-1} \text{ s}^{-1} \text{ cm}^{-2}$. For the $1:1:1$ flavor ratio at Earth that is assumed throughout this paper, 64% of the expected events would stem from electron neutrinos, 23% from tau neutrinos and 13% from muon neutrinos.

The flux estimate derived from sample Ib is compatible with the astrophysical flux derived in [11], taking into account the systematic uncertainties. The flux is higher than the upper limit found in a search for high-energy muon neutrinos with the larger IceCube-59 [28]. This is not necessarily a contradiction, since the upper limit is set under the assumption of an unbroken power law—a practical premise until measurements of high energetic neutrinos provide a handle on any cutoff in the spectrum. A nonequalized flavor ratio or a slightly different slope of the neutrino spectrum could explain this, too.

The results from samples Ia, Ib and II are consistent, with an excess appearing only towards larger energies. In addition, one can compare the overlap between the samples

as a cross-check. Because of the different energy thresholds, one expects sample II to be largely a subsample of Ia. However, due to the difference in selection criteria and general low efficiency of only ∼10% with which signal events are selected, a perfect overlap cannot be expected. We find that of the 14 events of sample II, seven are also contained in Ia, where the majority of the remaining have not passed the different containment cut. All three high-energy events of sample Ib are also contained in sample II. Only two of them are also in sample Ia.

VIII. SUMMARY

We have reported on a search for astrophysical and atmospheric neutrino-induced particle showers in the IceCube-40 detector. The data were taken between April 2008 and May 2009 with a total of 367.1 days live time.

Three different event selections, Ia, Ib and II, each tailored to different energy ranges, were developed and applied to the data. The low- and intermediate-energy samples Ia and II have an energy threshold of 2 and 25 TeV, respectively, and have sensitivity to atmospheric neutrinos. In both samples, an excess over the atmospheric muon background was observed that can be well explained by conventional atmospheric neutrinos.

With an energy threshold of 25 TeV, analysis II also has sensitivity to a high-energy astrophysical neutrino flux. In the absence of an excess of events above the combined background of atmospheric neutrinos and muons we are left

with an upper limit (90% confidence level) of $E^2\Phi_{\text{lim}} \leq 7.46 \times 10^{-8}$ GeV sr^{-1} s^{-1} cm^{-2} on the all-flavor astrophysical neutrino flux, assuming an E^{-2} spectrum and a $1:1:1$ neutrino flavor ratio at the Earth. For this limit, 90% of the expected signal events have energies in the range between 25 TeV to 5 PeV. The upper limit is below that reported from cascade searches using the IceCube-22 detector [40] and approaches the Waxman-Bahcall limit [5,6].

Finally, sample Ib was optimized towards the largest sensitivity for high-energy astrophysical neutrinos. Compared to sample II, it profited from a larger sample of simulated muon background during the optimization of the event selection. In 90% of the available data, three events were observed above the energy threshold of 100 TeV, with an expectation of only 0.25 events from atmospheric neutrinos (both conventional and prompt) as well as atmospheric muons—a 2.7σ excess. The 10% burn sample contains a fourth event, which has not entered the significance calculation.

The excess seen above 100 TeV in sample Ib is noteworthy. Although not significant enough to claim evidence for an astrophysical neutrino flux, it is consistent with similar excesses found in diffuse neutrino searches with IceCube-59 [28] using muon neutrino events, the two PeV events [10] and the 28 events found in [11], the strongest single evidence that IceCube is seeing a high-energy neutrino flux of astrophysical neutrinos. This analysis thereby provides three neutrino event candidates between 144 and 224 TeV—an intermediate energy scale—with unprecedented low background contamination of conventional atmospheric neutrinos and muons. The constraints on the all-flavor normalization of the high-energy neutrino flux of astrophysical neutrinos with equal flavor contributions are summarized in Fig. 13. A 90% credible interval covers the range $(2\text{–}14) \times 10^{-8}$ GeV sr^{-1} s^{-1} cm^{-2} and is compatible with the more stringent flux estimate established by [11].

However, the sensitivity towards a diffuse flux of high-energy neutrinos was reached using data from only 50% of the final IceCube configuration. It is the good energy resolution and the little intrinsic background associated with the signature of neutrino-induced cascades, that is thereby providing the large sensitivity to the diffuse flux [16]. The IceCube detector is now completed with 86 strings and an instrumented volume of 1 km^3. Future cascade searches benefit from the more favorable detector geometry, which allows for even better suppression of the background from atmospheric muons and improved cascade detection efficiency [17,18]. Neutrino-induced cascades will hence continue to play a prime role in further exploring the high-energy astrophysical neutrino flux.

APPENDIX: CALCULATION OF THE POSTERIOR PROBABILITIES

The experiment under consideration is a counting experiment in the presence of background. In order to incorporate systematic and statistical uncertainties into the interpretation of the result, a Bayesian approach was chosen. The probability to have observed n_{obs} events in the presence of n_{sig} events, signal selection efficiency ϵ and n_{bg} background events is given by the Poisson probability:

$$P(n_{\text{obs}}|n_{\text{sig}}, n_{\text{bg}}) = \frac{(\epsilon n_{\text{sig}} + n_{\text{bg}})^{n_{\text{obs}}}}{n_{\text{obs}}!} \exp\left(-(\epsilon n_{\text{sig}} + n_{\text{bg}})\right).$$

(A1)

From having observed n_{obs} we want to infer whether a given value of n_{sig} is supported or ruled out by the experimental result. This information is given by the posterior probability of n_{sig}, which can be obtained by applying Bayes theorem. In order to use the theorem, available information on the expected signal as well as the uncertainty of the other parameters must be quantified in the form of priors. By marginalizing over all parameters other than n_{sig}, remaining uncertainties are then incorporated into the final result.

The background uncertainties from model predictions and selection efficiencies are described by $p(n_{\text{bg}})$. For the signal we model all uncertainties with $p(\epsilon)$ and the prior belief with $p(n_{\text{sig}})$. The posterior probability can then be calculated:

$$P(n_{\text{sig}}|n_{\text{obs}}) \propto \int dn_{\text{bg}} d\epsilon P(n_{\text{obs}}|n_{\text{sig}}, n_{\text{bg}}) p(n_{\text{bg}}) p(\epsilon) p(n_{\text{sig}}).$$

$$(A2)$$

A constant is chosen for the signal prior to reflect no prior knowledge on the signal. For the background prior a Gaussian is used. The mean is centered at the rate

prediction, the width represents the modeled uncertainty and it is truncated at zero since rates have to be positive. The uncertainty in the signal efficiency is modeled with the factor ϵ that is applied to the number of signal events after all cuts. The prior for ϵ is modeled with a Gaussian centered at 1 and having a width corresponding to the systematic uncertainty. It is also truncated at zero.

[1] M. Ackermann *et al.*, Science **339**, 807 (2013).
[2] A. M. Hillas, arXiv:astro-ph/0607109.
[3] R. Abbasi *et al.*, Nature (London) **484**, 351 (2012).
[4] M. G. Aartsen *et al.*, arXiv:1307.6669 [Astrophys. J. (to be published)].
[5] E. Waxman and J. N. Bahcall, Phys. Rev. D **59**, 023002 (1998).
[6] E. Waxman, arXiv:1101.1155.
[7] H. Athar, M. Jezabek, and O. Yasuda, Phys. Rev. D **62**, 103007 (2000).
[8] J. F. Beacom, N. F. Bell, D. Hooper, S. Pakvasa, and T. J. Weiler, Phys. Rev. D **68**, 093005 (2003).
[9] T. Kashti and E. Waxman, Phys. Rev. Lett. **95**, 181101 (2005).
[10] M. G. Aartsen *et al.*, Phys. Rev. Lett. **111**, 021103 (2013).
[11] IceCube Collaboration, Science **342**, 1242856 (2013).
[12] R. Abbasi *et al.*, Phys. Rev. D **83**, 012001 (2011).
[13] M. G. Aartsen *et al.*, Phys. Rev. Lett. **110**, 151105 (2013).
[14] S. L. Glashow, Phys. Rev. **118**, 316 (1960).
[15] M. G. Aartsen *et al.*, arXiv:1305.6811.
[16] M. Kowalski, J. Cosmol. Astropart. Phys. 05 (2005) 010.
[17] A. Schönwald, A. M. Brown, and L. Mohrmann (IceCube Collaboration), *Proceeding of the 33rd International Cosmic Ray Conference, Rio de Janeiro, Brazil, 2013*; arXiv:1309.7003, pp. 29–32.
[18] M. Lesiak-Bzdak and A. Stößl (IceCube Collaboration), *Proceeding of the 33rd International Cosmic Ray Conference, Rio de Janeiro, Brazil, 2013*; arXiv:1309.7003, pp. 5–8.
[19] A. Achterberg *et al.*, Astropart. Phys. **26**, 155 (2006).
[20] R. Abbasi *et al.*, Nucl. Instrum. Methods Phys. Res., Sect. A **601**, 294 (2009).
[21] R. Abbasi *et al.*, Nucl. Instrum. Methods Phys. Res., Sect. A **618**, 139 (2010).
[22] A. Gazizov and M. Kowalski, Comput. Phys. Commun. **172**, 203 (2005).
[23] A. M. Dziewonski and D. L. Anderson, Phys. Earth Planet. Inter. **25**, 297 (1981).
[24] H. L. Lai, J. Huston, S. Kuhlmann, J. Morfin, F. Olness, J. F. Owens, J. Pumplin, and W. K. Tung, Eur. Phys. J. C **12**, 375 (2000).
[25] M. Honda, T. Kajita, K. Kasahara, S. Midorikawa, and T. Sanuki, Phys. Rev. D **75**, 043006 (2007).
[26] R. Enberg, M. H. Reno, and I. Sarcevic, Phys. Rev. D **78**, 043005 (2008).
[27] T. K. Gaisser, Astropart. Phys. **35**, 801 (2012).

[28] A. Schukraft, Nucl. Phys. B, Proc. Suppl. **237**–**238** 266 (2013).
[29] G. D. Barr, T. K. Gaisser, P. Lipari, S. Robbins, and T. Stanev, Phys. Rev. D **70**, 023006 (2004).
[30] D. Chirkin and W. Rhode, in Proceedings of ICRC 2001, Hamburg, Germany, 2001 (unpublished).
[31] B. Voigt, Ph.D. thesis, Humboldt-Universität zu Berlin, 2008, http://edoc.hu-berlin.de/dissertationen/voigt-bernhard-2008-07-16/PDF/voigt.pdf.
[32] L. Rädel and C. Wiebusch, Astropart. Phys. **44**, 102 (2013).
[33] Lisa Gerhardt and Spencer R. Klein, Phys. Rev. D **82**, 074017 (2010).
[34] M. Kowalski, Ph.D. thesis, Humboldt-Universität zu Berlin, http://edoc.hu-berlin.de/dissertationen/kowalski-marek-paul-2004-01-13/PDF/Kowalski.pdf.
[35] D. Chirkin, arXiv:hep-ph/0407078.
[36] D. Chirkin, Ph.D. thesis, University of California, Berkeley, 2003.
[37] D. Heck, G. Schatz, T. Thouw, J. Knapp, and J. N. Capdevielle, Wissenschaftliche Berichte, Report No. FZKA-6019, 1998.
[38] R. Glasstetter *et al.*, Wissenschaftliche Berichte, Report No. FZKA-6345E, 1999.
[39] J. R. Hörandel, Astropart. Phys. **19**, 193 (2003).
[40] R. Abbasi *et al.*, Phys. Rev. D **84**, 072001 (2011).
[41] J. Lundberg, P. Miočinović, K. Woschnagg, T. Burgess, J. Adams, S. Hundertmark, P. Desiati, and P. Niessen, Nucl. Instrum. Methods Phys. Res., Sect. A **581**, 619 (2007).
[42] N. Whitehorn, J. van Santen, and S. Lafebre, Comput. Phys. Commun. **184**, 2214 (2013).
[43] F. James and M. Roos, Comput. Phys. Commun. **10**, 343 (1975).
[44] M. G. Aartsen *et al.*, arXiv:1311.4767 [J. Instrum. (to be published)].
[45] R. Abbasi *et al.*, Astropart. Phys. **34**, 420 (2011).
[46] M. D'Agostino, Ph.D. thesis, University of California, Berkeley, 2009.
[47] J. Ahrens *et al.*, Nucl. Instrum. Methods Phys. Res., Sect. A **524**, 169 (2004).
[48] A. Hoecker, P. Speckmayer, J. Stelzer, F. Tegenfeldt, and H. Voss, *Proc. Sci.*, ACAT (**2007**) 040 [arXiv:physics/0703039].
[49] G. C. Hill and K. Rawlins, Astropart. Phys. **19**, 393 (2003).
[50] S. Hickford, Ph.D. thesis, University of Canterbury, 2012.
[51] M. Ackermann *et al.*, J. Geophys. Res. **111**, D13203 (2006).

[52] R. Abbasi *et al.*, "Study of South Pole Ice Transparency with IceCube Flashers," *Proceedings of the 32nd ICRC, Beijing, China, 2011*; R. Abbasi *et al.*arXiv:1111.2731.

[53] R. Gandhi, C. Quigg, M. H. Reno, and I. Sarcevic, Astropart. Phys. **5**, 81 (1996).

[54] A. Cooper-Sarkar and S. Sarkar, J. High Energy Phys. 01 (2008) 075.

[55] J. Lundberg, J. Conrad, W. Rolke, and A. Lopez, Comput. Phys. Commun. **181**, 683 (2010).

[56] A. D. Martin, M. G. Ryskin, and A. M. Stasto, Acta Phys. Pol. B **34**, 3273 (2003).

[57] R. Abbasi *et al.*, Phys. Rev. D **79**, 102005 (2009).

[58] M. C. Gonzalez-Garcia, M. Maltoni, and J. Rojo, J. High Energy Phys. 10 (2006) 075.